A&A, 707, A47 (2026)
https://doi.org/10.1051/0004-6361/202556826

Astronomy & Astrophysics

Asteroseismology of the ZZ Ceti star WD 1310+583 using the Transiting Exoplanet Survey Satellite

Zsófia Bognár[1,⋆], Murat Uzundag[2], Francisco C. De Gerónimo[3,4], Alejandro H. Córsico[3,4], James Munday[5], Ádám Sódor[1], and Sam D. Barber[6,7]

[1] Konkoly Observatory, HUN-REN Research Centre for Astronomy and Earth Sciences, MTA Centre of Excellence, H-1121 Budapest, Konkoly Thege Miklós út 15-17, Hungary
[2] Institute of Astronomy, KU Leuven, Celestijnenlaan 200D, B-3001 Leuven, Belgium
[3] Instituto de Astrofísica de La Plata, IALP (CCT La Plata), CONICET-UNLP, La Plata, Argentina
[4] Grupo de Evolución Estelar y Pulsaciones. Facultad de Ciencias Astronómicas y Geofísicas, Universidad Nacional de La Plata, Paseo del Bosque s/n, (1900) La Plata, Argentina
[5] Department of Physics, Gibbet Hill Road, University of Warwick, Coventry CV4 7AL, United Kingdom
[6] Department of Astronomy, University of Texas at Austin, Austin TX-78712, USA
[7] McDonald Observatory, Fort Davis TX-79734, USA

Received 11 August 2025 / Accepted 12 January 2026

ABSTRACT

Aims. By analysing the light curves of the ZZ Ceti star WD 1310+583, we aim to determine its pulsational frequencies and to give constraints on the main stellar parameters using asteroseismology.
Methods. We performed the Fourier analysis of the TESS light curves of WD 1310+583 and selected the possible pulsational modes. We also used spectroscopic data collected with the Cosmic Origins Spectrograph of the Hubble Space Telescope to give constraints for the asteroseismic analysis. We perform the latter with period-to-period fits using fully evolutionary white dwarf models.
Results. The star presented in this paper shows a particularly high number (41) of pulsational frequencies, which provides a potential opportunity for detailed asteroseismic investigations. We found a mean period spacing of ∼40.5 seconds, which allows us to state that the stellar mass of WD 1310+583 is larger than ∼0.57 $M_{\odot}$. We also attempted an asteroseismological analysis by performing period-to-period fits, but we were unable to find a single statistically significant asteroseismological solution. We adopted a tentative solution consisting of a white dwarf model with $M_{*} = 0.632\,M_{\odot}$, $T_{\rm eff} = 11\,702$ K, and an asteroseismic distance $d = 27.75^{+0.17}_{-0.15}$ pc, which is significantly smaller than the one predicted by Gaia ($d = 30.79 \pm 0.2$ pc). We also determined that the rotational period of our target is 1.18 d.

Key words. techniques: photometric – techniques: spectroscopic – stars: interiors – stars: oscillations – stars: individual: WD 1310+583 – white dwarfs

1. Introduction

ZZ Ceti stars, also known as DAV stars, are pulsating white dwarfs with hydrogen-dominated atmospheres. These stars exhibit low-amplitude multiperiodic brightness variations caused by non-radial g-mode oscillations with periods ranging from 100 to 1500 seconds. These pulsations are driven by a combination of the $\kappa-\gamma$ mechanism, operating within the partial ionisation zone of hydrogen (Dolez & Vauclair 1981; Winget et al. 1982), and the convective driving mechanism (Brickhill 1991; Goldreich & Wu 1999). With effective temperatures spanning 10 500–13 000 K, ZZ Ceti stars are confined to a well-defined region in the Hertzsprung–Russell diagram known as the ZZ Ceti instability strip.

As these stars cool across the instability strip, their pulsational properties vary systematically. Near the blue (hot) edge, they exhibit a lower number of pulsation modes with smaller amplitudes and shorter periods. Towards the red (cool) edge, the number of detectable modes increases, their amplitudes grow, and the pulsations become less stable, often showing amplitude and frequency variations on timescales of days to weeks (see e.g. Section 6 in Fontaine & Brassard 2008). Intriguingly, many cool ZZ Ceti stars also display episodic outbursts, characterised by brief and irregular increases in stellar brightness (see Bell et al. 2015, 2016, 2017; Bognár et al. 2023 and Hermes et al. 2015), which may provide insight into the interaction between pulsation and convection.

ZZ Ceti stars are invaluable astrophysical laboratories for investigating the physics of dense matter under extreme conditions. Their small size (approximately Earth-like) and high surface gravity ($\log g \sim 8$) result in strongly stratified atmospheres, where heavier elements settle below a hydrogen or helium layer due to gravitational separation. These characteristics make them ideal for asteroseismology, a technique that uses observed pulsation periods to infer the star's internal structure, chemical composition, and rotational properties. Such studies contribute to understanding stellar evolution and the formation of compact objects (Winget & Kepler 2008; Fontaine & Brassard 2008; Althaus et al. 2010; Córsico et al. 2019; Córsico 2020).

Recent advances in space-based photometry, particularly with the Transiting Exoplanet Survey Satellite (TESS; Ricker et al. 2015), have revolutionised the study of ZZ Ceti stars. TESS provides high-precision, high-cadence observations, enabling detailed frequency analyses and the detection of new

⋆ Corresponding author: bognar.zsofia@csfk.org

pulsation modes, even in stars previously deemed observationally challenging. This has opened new avenues for understanding the global properties of white dwarfs and the underlying physics driving their pulsations (Bell et al. 2019; Bognár et al. 2020).

The brightness variations of the ZZ Ceti star WD 1310+583 were independently discovered by Gentile Fusillo et al. (2018) and Bognár et al. (2018). The latter study presents photometric investigations conducted at the Konkoly Observatory (Hungary). Seven independent modes were identified on the basis of the datasets. In the study by Gentile Fusillo et al. (2018), two possible pulsation frequencies were published as a result of their analysis. The star has been independently suggested as a double degenerate source based on spectroscopic or hybrid (photometric, spectroscopic plus astrometric data) fits using ultraviolet (Gentile Fusillo et al. 2018) and optical (Munday et al. 2024) spectroscopy. Munday et al. (2024) found little radial velocity variability, indicating that the source is likely a wide double white dwarf binary star system.

In this paper, we focus on the TESS measurements of WD 1310+583. First, we analyse the spectroscopic data available on WD 1310+583, then we present the TESS datasets to identify the pulsation modes of this star. Using these findings, we estimate the period spacing to constrain the stellar mass of WD 1310+583 and attempt an asteroseismic investigation to constrain its global parameters and internal structure.

2. Spectroscopic analysis

In the following, we present the results of the system parameters of a double-degenerate fit to the spectra obtained on WD 1310+583 (TIC 157271533, $G = 14.07$ mag, $\alpha_{2000} = 13^{h}12^{m}58^{s}$, $\delta_{2000} = +58^{d}05^{m}11^{s}$). At the time of writing, precise Gaia parallax measurements were not available to Gentile Fusillo et al. (2018), and the authors chose to fix the surface gravity of both stars to $\log g = 8.0$ dex when producing the atmospheric parameters of the two stars. With that in mind and to obtain an improved spectroscopic solution to the ultraviolet data, we decided to refit their Hubble Space Telescope Cosmic Origins Spectrograph (HST COS) spectrum with new information at hand, utilising all-sky photometry and Gaia parallaxes to give absolute flux measurements.

We used the WD-BASS pipeline (Munday et al. 2024) with Pan-STARRS all-sky photometry (Chambers & Pan-STARRS Team 2018, filters *grizy*), the Sloan Digital Sky Survey (filters *ugriz*) DR16 (Ahumada et al. 2020), and the Gaia data release 3 (DR3) parallax of $\pi = 32.48 \pm 0.25$ mas. We fitted the wavelength range of 1200–1930 Å, trimming the very low signal-to-noise data. We masked geocoronal lines between vacuum wavelengths 1206–1226 Å, 1295–1315 Å, and also within 1 Å of all entries supplied in the line list of Sahu et al. (2023) to ignore any potential undesired photospheric and/or interstellar flux contribution.

Synthetic spectra were obtained by interpolating the 3D local thermodynamic equilibrium grids of Tremblay et al. (2013, 2015) for DA white dwarfs, which are based on the line profiles of Tremblay & Bergeron (2009). The hotter star, which dominates the flux, has Balmer absorption lines and is clearly a DA, but the spectral class of the secondary star is unknown since it exhibits no unique spectral lines. Hence, the dimmer companion could be a helium-atmosphere DC, and in testing this DA plus DC combination, we interpolate synthetic spectra from Cukanovaite et al. (2021). The temperature, surface gravity, and radial velocity of the two stars and the parallax of the system were independent variables in the fitting. We used the mass–temperature–radius relationships from the hydrogen-rich (DA) and helium-rich (DC) evolutionary sequences of Bédard et al. (2020) to obtain stellar radii and calculate the luminosity of each star. Observations were scaled from an Eddington flux to an observed flux using the reciprocal of the parallax as the distance in parsecs, with an extinction coefficient of $E(B-V) = A_V/R_V = 0.01/3.1$ applied to redden the synthetic spectra (Gentile Fusillo et al. 2021). No spectrum normalisation was applied; the observed flux in physical units was fitted in both the HST COS spectrum and the all-sky photometry with a common parallax measurement to each dataset. A Gaussian prior was placed on the fitted parallax using the parallax, and the error reported in Gaia DR3.

Table 1. Physical parameters of different spectroscopic fits.

DA+DA fit	
T_1 =	11 670 ± 163 K
$\log g_1$ =	8.13 ± 0.04 dex
T_2 =	8240 ± 115 K
$\log g_2$ =	8.09 ± 0.04 dex
Fitted Parallax =	31.75 ± 0.17 mas
DA+DC fit	
T_1 =	11 650 ± 163 K
$\log g_1$ =	8.12 ± 0.04 dex
T_2 =	7540 ± 106 K
$\log g_2$ =	7.78 ± 0.04 dex
Fitted Parallax =	31.56 ± 0.17 mas

Notes. For more reflective errors including systematics, we present external errors of 1.4% for $T_{\rm eff}$ and 0.042 dex for $\log g$, respectively (Liebert et al. 2005).

However, as it turns out, we need to be careful with the automatic use of the Gaia parallax. The value of the parameter of the renormalised unit weight error (RUWE) for WD 1310+583 (Gaia DR3 1566603962760532736) is quite high: 16.315. This may also indicate the presence of a binary star system, as the RUWE parameter measures the goodness of an astrometric fit to the data (see e.g. Castro-Ginard et al. 2024). We checked the Gaia DR3 database (Gaia Collaboration 2022) and found that the parameter `astrometric_excess_noise` is 2.688 mas, the `astrometric_excess_noise_sig` is 4076, and the `visibility_periods_used` is 28. It strongly indicates that the 'single-star' astrometric model is not adequate: the high RUWE and, in particular, the large `astrometric_excess_noise`, together with its extreme significance, show that the assumed single-star model fails to explain many of the measurements. The most likely physical cause is photocentre motion (e.g. due to a close binary, an unresolved companion, or blending) or strong photometric variability that shifts the astrometric positions. Thus, the parallax may be inaccurate or partially biased (the formal `parallax_error` is likely too optimistic). We must bear in mind that it is not recommended to use the value of 32.48 mas automatically as an accurate distance estimate; however, this is currently the best-known estimate of the star's distance. The `visibility_periods_used = 28` shows that there was a sufficient number of observations, so the poor fit is not simply due to a small data sample; the deviation is real.

The best-fit solutions are shown in Figs. 1 and 2, respectively, while the physical parameters of the different solutions can be seen in Table 1. As in Gentile Fusillo et al. (2018), we conclude that a single star solution does not suffice to model

Table 2. Journal of observations of WD 1310+583.

Object	TIC ID	Start time (BJD-2 457 000)	N	δT (d)	G mag	Sect. (Cadence)	CROWDSAP
WD 1310+583	157271533	1711.362	29 058	51.2	14.1	15–16 (120 s)	0.99
		1900.094	16 326	26.4		22 (120 s)	
		2610.234	28 155	54.1		48–49 (120 s)	
		3339.788	21 531	55.0		75–76 (120 s)	

Notes. TIC ID refers to TESS Input Catalog identifier of object, N is number of data points after cleaning light curve, δT is total length of datasets including gaps, and Sect. is serial number of sector(s) in which star was observed. The start time in BJD is the time of the first data point in the dataset. The CROWDSAP keyword represents the ratio of the target flux to the total flux in the TESS aperture. We note that here we list the CROWDSAP value from the first TESS run.

WD 1310+583. The flux contributed by the companion in the ultraviolet is small, but the relative flux contribution from the companion becomes significant towards redder wavelengths. As such, the companion star serves as an extra flux contributor, and there is no way to decisively reveal its spectral type. For this reason, both combinations of DA plus DA and DA plus hydrogen-deficient DC are presented. Crucially, since the flux in the ultraviolet almost completely originates from the hotter object, the atmospheric parameters of the pulsating white dwarf are near identical across the two models, meaning that the unknown combination of DA plus DA or DA plus DC does not noticeably impact our astroseismetric analysis.

3. Light curve analyses of the TESS observations

TESS measured the star in 120-second short-cadence mode in these sectors: 15, 16, 22, 48, 49, 75, and 76. Measurements are also available in 20-second ultra-short cadence mode, but we did not see peaks above the Nyquist frequency of the 120-second measurements. So, we examined the 120-second measurements more closely.

First, we performed frequency analyses for sectors s15s16, s22, s48s49, and s75s76 using the photometric module of the Frequency Analysis and Mode Identification for Asteroseismology (FAMIAS) software package (Zima 2008). As seen, we treated the data of the neighbouring sectors jointly. For frequency analyses, we set the significance limit at 0.1% false alarm probability (FAP). We created a table of the observed peaks in the different sectors and considered the peaks that are approximately at the same frequency in the different datasets as the same frequency. The full list of detected frequencies can be found in the tables of Appendix B. After we identified the common frequencies and their amplitudes provided by the analyses, we calculated the amplitude-averaged period value for each frequency. A total of 67 frequencies were detected in the individual datasets. Based on pairwise frequency separations, 39 pairs with spacings smaller than 1.22 μHz were identified. Since all remaining pairs are separated by at least 2.70 μHz, we adopted 1.22 μHz as the threshold below which the frequencies were combined by means of a weighted average.

We also checked for the presence of linear combinations in each dataset. There are groups of peaks above about 700 s, and we considered the one with the highest amplitude as the representative frequency of the given frequency group. Table 2 summarises the journal of observations, while Appendix A lists the frequencies, periods, and amplitudes of the peaks detected by the analysis of the datasets from the different sectors. The comparison of the Fourier spectra of the different segments of the light curve is shown in Fig. 3.

4. Rotational multiplets

The equation we used to calculate the rotation period of the star is as follows (see e.g. the Appendix in Winget et al. 1991):

$$\delta f_{k,l,m} = m(1 - C_{k,l})\Omega, \quad (1)$$

where k, l, and m are the radial order, horizontal degree, and azimuthal order of the non-radial pulsation mode, respectively. The coefficient $C_{k,l}$ can be calculated as $C_{k,l} \approx 1/\ell(\ell+1)$. This relation is valid for high-overtone ($k \gg \ell$) g-modes; Ω is the (uniform) rotational frequency.

Examining the frequencies listed in Appendix A reveals the presence of possible rotational triplet and doublet frequencies separated by approximately 5 and 10 μHz, respectively. The 10 μHz separations may correspond to triplets with 5 μHz frequency differences. A total of eight doublets were identified, as summarised in Fig. 4 and Table 3. Assuming that all are $l = 1$ modes and that the average frequency separation is 4.9 μHz, the star's rotational period is calculated to be P = 1.18 d, considering Eq. (1). This value is in good agreement with the hour-to-day rotation periods typically observed in pulsating white dwarf stars; see, for example, Section 7 in Hermes et al. (2017).

5. Period spacing tests

Here, our primary goal is to deepen our understanding of stellar structure, particularly the mass of the observed object. We note that the photometric and spectroscopic masses are in good agreement, as shown in Table B.1. of the following work: Calcaferro et al. (2024). The mean period spacing serves as an indicator of the stellar mass. We conducted several tests, as follows: using a subset of the periods listed in Appendix A, we searched for a characteristic period spacing using Kolmogorov-Smirnov (K-S; Kawaler 1988) and inverse variance (I-V; O'Donoghue 1994) significance tests. In the K-S test, the quantity Q represents the probability that the observed periods are randomly distributed. A characteristic period spacing in the period spectrum would manifest itself as a minimum in Q. Meanwhile, in the I-V test, a maximum indicates the presence of a constant period spacing. Another widely recognised approach to identifying a characteristic spacing value is performing a Fourier analysis on a Dirac comb constructed directly with periods (e.g. Winget et al. 1991; Handler et al. 1997).

Fig. 5 shows the results of applying the statistical tests to a subset of 11 periods detected in WD 1310+583. These periods are marked with an asterisk in Appendix A. The three tests reveal a clear period spacing of 40.58 s, which can be associated with modes that have $\ell = 1$. A spacing of ~20 seconds is also observed in the three tests. This corresponds to the subharmonic of the spacing ($\Delta\Pi/2$). Using a linear least-squares

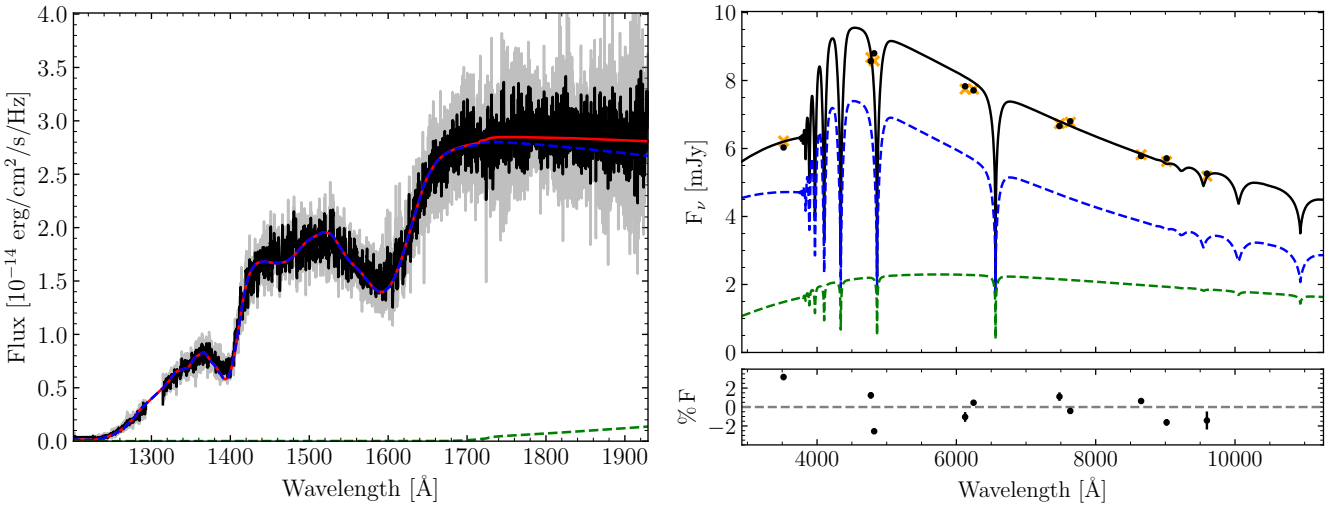

Fig. 1. Best-fitting solution for DA plus DA two-star model. Left panel: Fit to the HST COS spectrum. Right panel: Solution with photometric data. The synthetic flux from the hotter, pulsating white dwarf is shown in dashed blue while the flux from the cooler companion is shown in dashed green. In the left panel, the reduced spectrum is in grey, and the smoothed spectrum (across five data points) is in black. In the right panel, the synthetic flux in each filter is given as black circles, and the orange crosses are observed fluxes from the photometric surveys, with the percentage flux residual underneath. The total flux is in red on the left and black on the right for clarity.

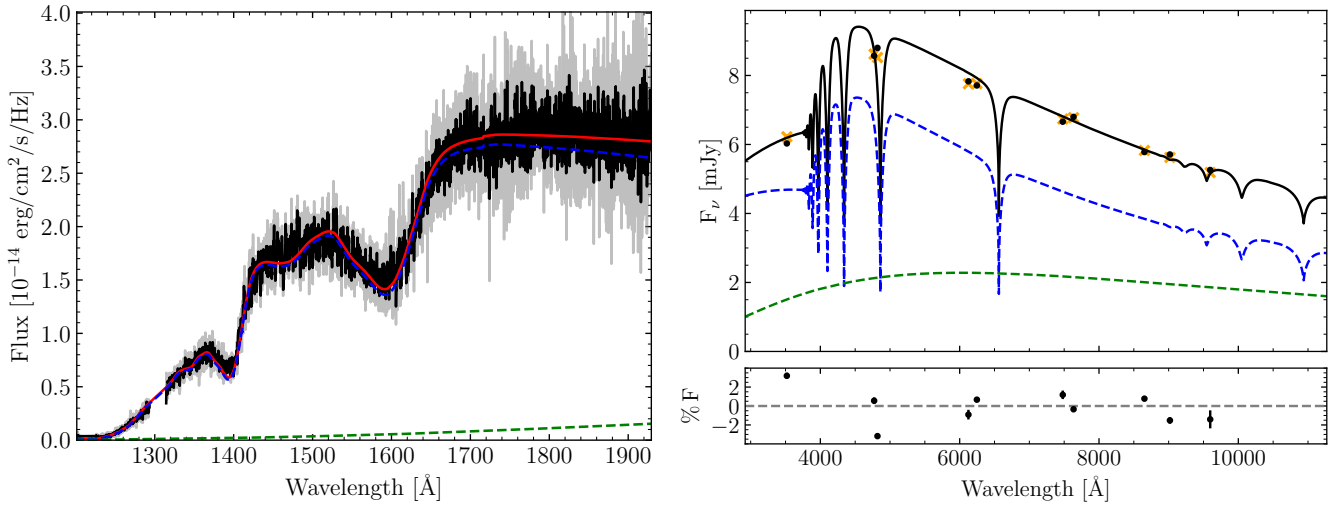

Fig. 2. As for Fig. 1 but for a DA plus DC two-star model. See Sect. 2 for more details.

fit to the identified dipole modes, we derive a mean period spacing of $\Delta\Pi_{\ell=1} = 40.51$ s (see Fig. 6). To robustly estimate the associated uncertainty, we adopted the error-propagation method described by Uzundag et al. (2023), which is based on the approach of Uzundag et al. (2021). This method involves generating 1000 random permutations of the observed periods, in each case assigning a value of $m \in \{-1, 0, +1\}$ for triplets (and $m \in \{-2, -1, 0, +1, +2\}$ for quintuplets) to all detected modes. Then each set is adjusted to the intrinsic $m = 0$ component assuming rotational splitting, and a new linear fit is performed. The uncertainty in the mean period spacing is taken as the standard deviation of the resulting distribution of best-fit slopes, yielding $\Delta\Pi_{\ell=1} = 40.51^{+1.99}_{-1.96}$ s. The residuals of the observed periods relative to this mean period spacing (lower panel of Fig. 6) clearly reveal deviations consistent with mode trapping signatures in the pulsation spectrum of WD 1310+583. The discovery of the period spacing $\Delta\Pi_{\ell=1}$ allows the harmonic degree $\ell = 1$ to be assigned to the 11 periods that make up the sequence, allowing strong constraints to fits of individual periods to be placed (see Section 6.2).

In summary, we first used rotational multiplets to identify the most secure modes. These identifications then served as priors when we searched for the asymptotic period-spacing pattern. We applied this procedure consistently. The two methods are not in conflict; they are complementary.

6. Asteroseismology

All of our efforts to determine the independent pulsation modes were to provide these modes for the asteroseismic analysis of the star presented in the following sections. We begin with the determination of the stellar mass using the identified period spacings and then proceed to present the results of the asteroseismic period-to-period fits.

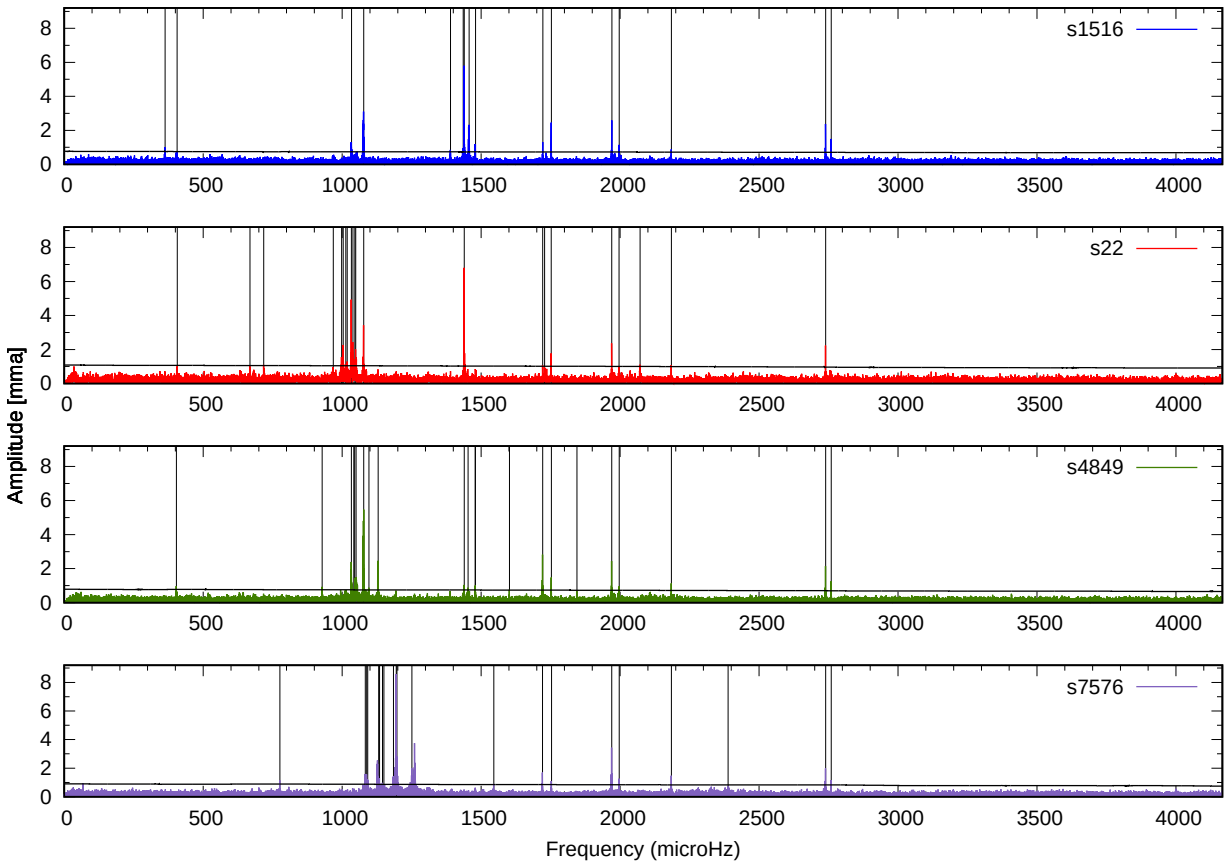

Fig. 3. Fourier spectra of different light curve segments. The horizontal black lines indicate the significance levels corresponding to a 0.1% FAP for each dataset. Amplitude variations are clearly visible from sector to sector. The vertical lines in each panel correspond to the frequencies listed in Appendix B.

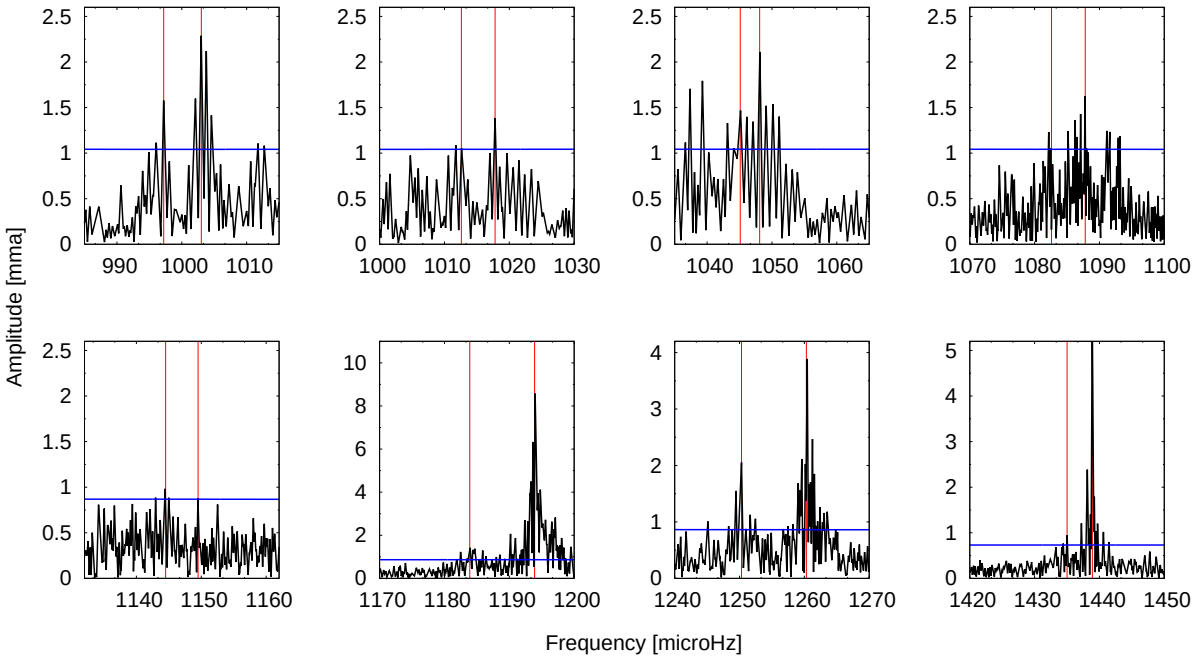

Fig. 4. Fourier spectra of possible rotational frequencies listed in Table 3. We note that we utilised pre-whitened Fourier spectra for the plots, as the lower-amplitude peaks become more clearly visible after pre-whitening. The horizontal blue lines indicate the significance levels corresponding to a 0.1% FAP for each dataset.

Table 3. Possible rotational doublet frequencies.

f [μHz]	δf [μHz]
997.2	
1003.0	5.8
1012.6	
1017.8	5.2
1044.8	
1048.6	3.8
1082.6	
1087.8	5.2
1144.5	
1149.5	5.0
1183.9	
1193.9	10.0
1250.3	
1260.3	10.0
1435.0	
1438.9	3.9

Notes. We also mark frequency differences in second column.

6.1. The stellar mass of WD 1310+583 as predicted by the observed period spacing

A practical approach to estimating the stellar mass of pulsating WD (white dwarf) stars involves comparing the observed period spacing ($\Delta\Pi$) with the average of the calculated period spacings ($\overline{\Delta\Pi_k}$) (Córsico et al. 2019). The average is determined using the formula $\overline{\Delta\Pi_k} = (n-1)^{-1} \sum_k \Delta\Pi_k$, where 'forward' period spacing ($\Delta\Pi_k$) is defined as $\Delta\Pi_k = \Pi_{k+1} - \Pi_k$ (with k representing the radial order) and n is the number of periods computed that fall within the range of observed periods. It is important to note that this method for determining stellar mass depends on the spectroscopic effective temperature, and the results are inevitably influenced by the uncertainties associated with $T_{\rm eff}$. The method mentioned leverages the fact that, in general, the period spacing of pulsating WD stars is mainly influenced by stellar mass and effective temperature, with only a minor dependence on the thickness of the He envelope for DBV stars or the O/C/He envelope for GW Vir stars (see e.g. Tassoul et al. 1990). However, this technique cannot be directly applied to DAV stars for mass estimation, as the period spacing in these stars is influenced by $M_\star$, $T_{\rm eff}$, and the mass of the H envelope $M_{\rm H}$, with similar sensitivity, leading to multiple combinations of these three parameters that yield the same period spacing. Therefore, we can only provide a possible range of stellar masses for WD 1310+583 based on the period spacing.

We calculated the mean of the period spacings for $\ell = 1$, denoted as $\overline{\Delta\Pi_k}$, employing the LP-PUL pulsation code (Córsico & Althaus 2006), in terms of the effective temperature across all the stellar masses considered and the thicknesses of the H envelope (see Table 4 of Uzundag et al. 2023). The analysed period range was established between 300 and 1600 seconds, encompassing the typical periods observed in the target star

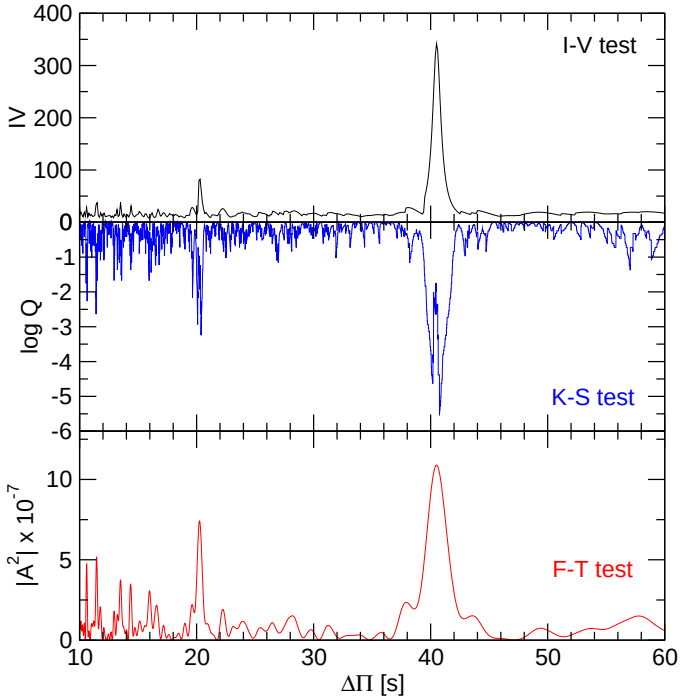

Fig. 5. Results of inverse variance (I-V, black), Kolmogorov-Smirnov (K-S, blue), and Fourier Transform (F-T, red) statistical tests applied to subset of 11 periods marked with asterisks in Appendix A. The three tests point to the existence of a period spacing of 40.58 s in WD 1310+583, which can be associated to $\ell = 1$ modes. The presence of the subharmonic of this spacing at ~20 seconds is also apparent.

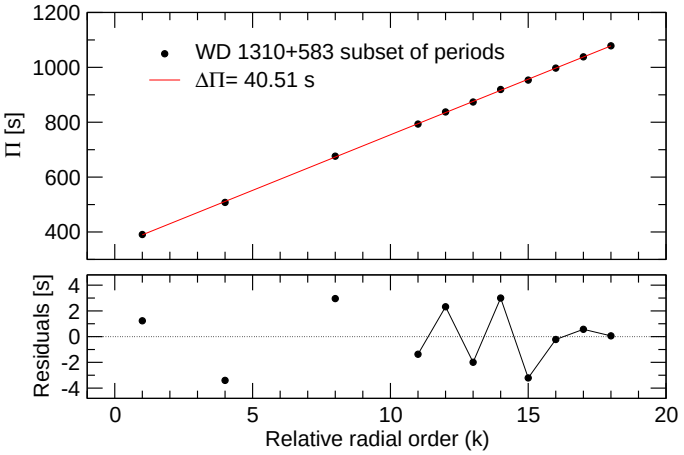

Fig. 6. Upper panel: Linear least-squares fit to 11 periods of WD 1310+583 marked with asterisks in Appendix A. The derived period spacing from this fit is $\Delta\Pi_{\ell=1} = 40.51$ s. Lower panel: Residuals of the period distribution relative to the mean period spacing, revealing signals of mode trapping in the period spectrum of WD 1310+583. Modes with a consecutive radial order are connected with thin black lines.

WD 1310+583. The effective temperature of WD 1310+583 according to this work (see Sect. 2) is $T_{\rm eff} = 11\,660 \pm 163$ K on average. However, there are other measurements of $T_{\rm eff}$ for this DAV star in the literature, such as $T_{\rm eff} = 10\,131 \pm 260$ K (Leggett et al. 2018), $T_{\rm eff} = 10\,313 \pm 111$ K (O'Brien et al. 2024), $T_{\rm eff} = 11\,617 \pm 70$ K (Gentile Fusillo et al. 2018), and $T_{\rm eff} = 11\,600 \pm 200$ K (Munday et al. 2024). In particular, the value of $T_{\rm eff}$ derived in the present study is almost the same as the val-

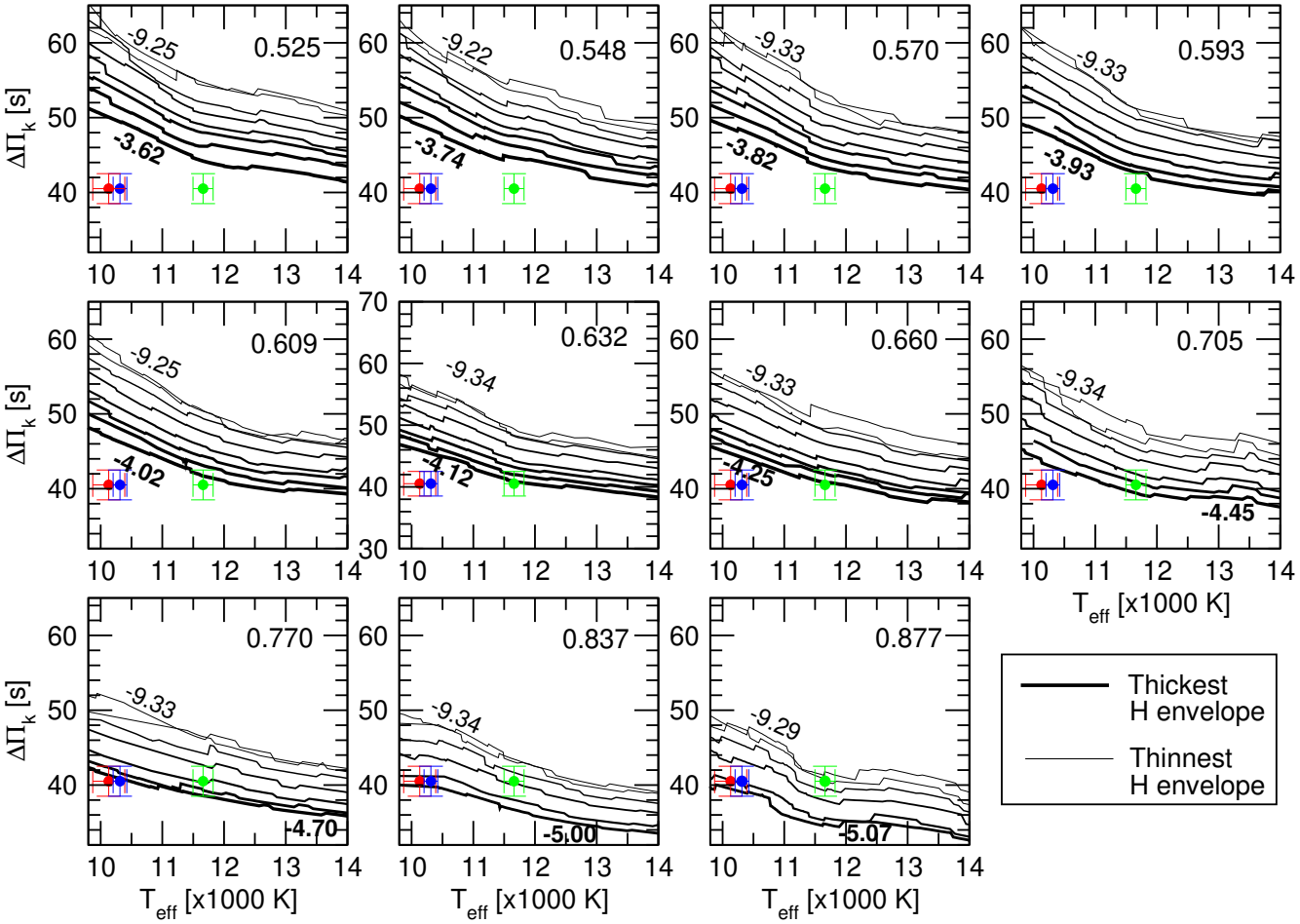

Fig. 7. Average of computed dipole ($\ell = 1$) period spacings, $\overline{\Delta\Pi_k}$, in terms of effective temperature, for different stellar masses in solar units (numbers at top right corner of each panel) and thicknesses of H envelope (see Table 4 of Uzundag et al. 2023, for the specific values of $\log(M_H/M_\star)$) drawn with different colours. In each panel, we include numbers along two curves, which correspond to the value of $\log(M_H/M_\star)$ for the thickest and the thinnest H envelopes for each stellar mass value. The location of WD 1310+583 is emphasized with a circle with error bars with effective temperatures $T_{\rm eff} = 10\,131 \pm 260$ K (red symbol; Leggett et al. 2018), $T_{\rm eff} = 10\,313 \pm 111$ K (blue symbol; O'Brien et al. 2024), and $T_{\rm eff} = 11\,660 \pm 163$ K (green symbol; Section 2 of this work), and a period spacing $\Delta\Pi = 40.51 \pm 2.00$ s (Section 5).

ues derived by Gentile Fusillo et al. (2018) and Munday et al. (2024).

As there is no definitive effective temperature measurement available for this star, we used multiple estimates to cover the possible range of $T_{\rm eff}$. The results are illustrated in Fig. 7, showing $\overline{\Delta\Pi_k}$ for various stellar masses (specified at the top right corner of each panel), represented by curves with different thicknesses corresponding to the diverse values of M_H. To enhance clarity, we only labelled the extreme H-envelope thickness values for each stellar mass, using thick and thin black curves. The position of WD 1310+583, marked by a small circle with error bars, was examined with three spectroscopic effective temperature values: $T_{\rm eff} = 10\,131 \pm 260$ K (Leggett et al. 2018), $T_{\rm eff} = 10\,313 \pm 111$ K (O'Brien et al. 2024), representative of most of the $T_{\rm eff}$ determinations, which point to low effective temperatures, and $T_{\rm eff} = 11\,660 \pm 163$ K (this paper), along with a period spacing of $\Delta\Pi = 40.51 \pm 0.14$ s.

Upon analysis of the plot, we infer that, based on the period spacing and $T_{\rm eff}$, the stellar mass of WD 1310+583 likely falls between 0.570 $M_\odot$ (with a thick H envelope of $\log(M_H/M_\star) = -3.82$) and 0.877 $M_\odot$ (with a very thin H envelope of $\log(M_H/M_\star) = -9.29$) if the effective temperature is high (green dot in Fig. 7). In contrast, if the effective temperature of WD 1310+583 is lower (as indicated by the red and blue dots in Fig. 7), then the stellar mass would probably exceed 0.705 $M_\odot$ with a thick envelope of H ($\log(M_H/M_\star) = -4.45$). In summary, based on the period spacing and effective temperature, the stellar mass of WD 1310+583 would be higher than ~0.57 $M_\odot$.

6.2. Asteroseismic period-to-period fits

In this section, we try to find an evolutionary model that best matches the theoretical periods with the individual pulsation periods detected for WD 1310+583. The quality of the fit is assessed by evaluating the quality function defined as follows:

$$\sigma^2(M_\star, M_H, T_{\rm eff}) = \frac{1}{N}\sum_{i=1}^{N} \min[(\Pi_i^{\rm O} - \Pi_k^{\rm th})^2]. \quad (2)$$

Here, N represents the number of detected modes, $\Pi_i^{\rm O}$ are the observed periods, and $\Pi_k^{\rm th}$ are the theoretically computed periods (where k is the radial order). The best-fitting model, if it exists, is chosen by identifying the minimum value of σ^2.

We use the same grid of CO-core WD models as in Uzundag et al. (2023), which contemplates evolutionary

Table 4. Parameters of the best-fit models.

Model #	$M_\star$ ($M_\odot$)	$\log g$ (cm s^{-2})	$T_{\rm eff}$ (K)	$\log\left(\frac{M_{\rm H}}{M_\star}\right)$	$\sigma^2(s^2)$	$\ell = 1$	d (pc)
1	0.609	8.03	11 441	–4.02	26.52	21	27.65
2	0.837	8.39	11 147	–5.35	27.07	19	20.74
3	0.632	8.06	11 702	–5.35	26.03	22	27.75

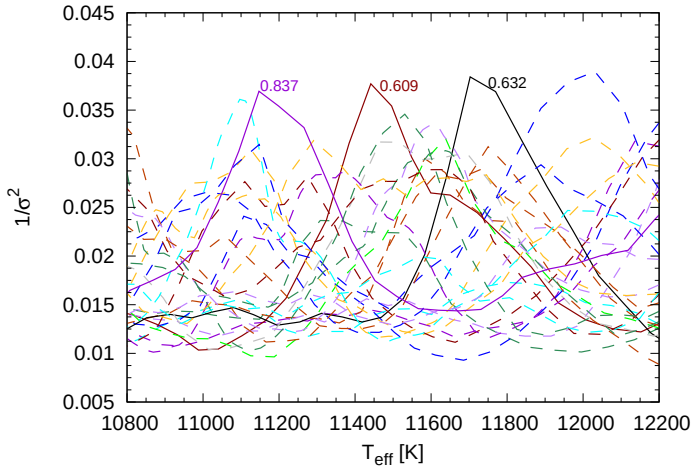

Fig. 8. Inverse of squared quality as function σ defined in Eq. (2) in terms of effective temperature. Solid (dashed) lines represent the value for the selected (discarded) models (see Table 4).

sequences of stellar masses in the range $0.525 \leq M_\star/M_\odot \leq 0.877$, with effective temperature $10\,000\,\mathrm{K} \leq T_{\rm eff} \leq 13\,000\,\mathrm{K}$, and varying the total hydrogen content $-9 \lesssim \log(M_{\rm H}/M_\star) \lesssim -4$. For the period-to-period fit, we examined the frequency spectrum of WD 1310+583 and used the confirmed triplets and the consecutive overtones derived as $\ell = 1$ as input priors; see Appendix A and Table 3. We considered the central components (with $m = 0$), specifically the eight observed periods (793.4, 837.6, 873.8, 919.3, 953.6, 997.1, 1038.4, and 1078.4 s), which were assigned $\ell = 1$ for the analysis.

In Fig. 8 we show the value of the inverse of the squared quality function for our models, in the range of effective temperatures of interest. With solid lines, we highlight the quality function for the models that best match the observed periods, as indicated by the maximum in the curve. The two models represented by the maxima of the dashed blue (cyan) curves next to the solid curves were discarded because of their hot (cold) effective temperatures. The three best-fit models highlighted represent only marginally better fits than other models, which prevents us from considering them as seismic measurements of the properties of WD 1310+583. Indeed, the three individual highest peaks are not statistically compelling enough for their parameters to be worth discussing as properties of this star. In view of this, from now on we limit ourselves to describing the properties of tentative seismological solutions for WD 1310+583.

The most important stellar parameters of our tentative asteroseismic models are shown in Table 4. Given the $T_{\rm eff}$ values obtained in this work, which considers the binary nature of this system, we focus our analysis in the vicinity of $T_{\rm eff} \sim 11\,600$ K. Based on our results, it is more likely that WD 1310+583 would have a thick H-envelope. However, the more massive solution exhibits a significant discrepancy with our spectroscopic determination of $\log g$ and the Gaia distance; therefore, we reject this model as a possible solution.

Always bearing in mind that none of these solutions is formally statistically significant, we can consider model 3 as a possible description of the structure of WD 1310+583 since its mass aligns with the results of the mean period spacing analysis and provides the best agreement between the theoretical and observed periods. Our tentative asteroseismological model is characterised by total H- and He-content of $4.46 \times 10^{-6}\,M_*$ and $1.75 \times 10^{-2}\,M_*$, respectively, and a luminosity of $\mathrm{L/L_\odot} = 0.25 \times 10^{-2}$. We derived the internal uncertainties in the most important stellar parameters from the model grid resolution $\chi_{M_\star} = 0.028\,M_\odot$, $\chi_{T_{\rm eff}} = 70$ K, $\chi_{\log g} = 0.05$, $\chi_{L_\star/L_\odot} = 2 \times 10^{-4}$, and $\chi_{R_\star/R_\odot} = 1.2 \times 10^{-4}$.

Based on the stellar parameters derived from our tentative representative model, we estimate the asteroseismic distance of WD 1310+583. From the derived effective temperature and the logarithm of surface gravity, we calculated the absolute magnitude in the Gaia G band (D. Koester, personal communication). For the model with a mass of $0.632\,M_\odot$, we find that the absolute magnitude is $M_{\rm G} = 11.85$ mag. From the apparent magnitude obtained by the Gaia DR3 Archive[1] for WD 1310+583 ($m_{\rm G} = 14.07$ mag), we obtain an asteroseismic distance of $d = 27.75^{+0.17}_{-0.15}$ pc. We found that our distance is appreciably smaller compared to the Gaia distance (Bailer-Jones et al. 2021), which reports $d = 30.79 \pm 0.2$ pc.

7. Discussion

WD 1310+583 was one of the targets observed from the Konkoly Observatory as part of a survey aimed at discovering new pulsating white dwarf stars potentially detectable by TESS (see Bognár et al. 2018). This study presented observations obtained over eight nights, complemented by a preliminary asteroseismic analysis of the star. They identified 17 significant frequencies, seven of which were found to be independent pulsation modes, as also summarised in the introduction of this paper. Preliminary asteroseismic modelling was performed for six of these modes using the White Dwarf Evolution Code (WDEC; see Bischoff-Kim et al. 2008). Four of the six modes were also detected in the TESS data, within the limits of the observational uncertainties.

The preliminary asteroseismic analysis presented by Bognár et al. (2018) aimed to constrain the stellar mass, the effective temperature, and the mass of the hydrogen layer. Adapting the observed periods for six modes and assuming that at least four of them, including the dominant one, correspond to dipole modes ($\ell = 1$), the following parameters were derived: $M_* = 0.74\,M_\odot$, $T_{\rm eff} = 11\,600$ K, and $-\log M_{\rm H} = 4.0$. This mass is approximately $0.1\,M_\odot$ higher than that obtained from fully

[1] https://gea.esac.esa.int/archive/

evolutionary models (this work), while the hydrogen layer mass is roughly two orders of magnitude higher. However, the effective temperatures derived from the two modelling approaches are quite similar (11 600 K vs 11 702 K).

Bognár et al. (2018) also reported possible values of the rotational frequency splittings and the corresponding rotation periods. The stellar rotation period could be either 5 h or 1.3 d. It should be noted that the latter value is very close to the 1.18 d obtained from the TESS measurements.

The comparison between our asteroseismic results and previous analyses highlights the typical challenges in reconciling spectroscopic and seismological determinations of white dwarf parameters, particularly for DAVs (see Calcaferro et al. 2024). In this case, the asteroseismic mass derived from WDEC modelling exceeds the spectroscopic mass by about 0.1 $M_{\odot}$, a discrepancy that falls within the range commonly observed in pulsating DAs. Such differences may arise from systematic uncertainties that affect both methods. Spectroscopic parameters ($T_{\rm eff}$, $\log g$) depend on the atmosphere models adopted and the treatment of line broadening and convection, which significantly influence the Balmer line profiles (Saumon et al. 2022). As shown by Fuchs (2017), unaccounted for systematics such as imperfect flux calibration, extinction corrections, or low signal-to-noise ratios can introduce biases in $T_{\rm eff}$ and $\log g$, thereby affecting the derived masses. On the other hand, asteroseismic masses depend sensitively on mode identification and on the adopted model grids and internal chemical stratification profiles (De Gerónimo et al. 2018, 2017). For WD 1310+583, the assumption that most detected modes correspond to $\ell = 1$ may have influenced the stellar structure parameters of our tentative asteroseismological model, since even a small number of $\ell = 2$ modes can alter the inferred mass and thickness of the hydrogen layer.

We also emphasise that, as Fig. 8 clearly shows, our selected model is only a tentative solution. The best-fit models are only marginally better fits than the other models, which means that the models presented in Table 4 are not statistically significant, so we cannot find a robust seismological solution. Although the star shows a rich pulsation spectrum with robustly identified modes, this does not mean that we can find a representative model, highlighting the need for improvements on the modelling side and the asteroseismological method employed, as also discussed in Calcaferro et al. (2024).

Our analysis of WD 1310+583 exemplifies the broader trend observed among DAVs, where the spectroscopic mass may overestimate or underestimate the seismological mass depending on the interplay of uncertainties in both approaches. The degeneracy between the core and envelope structure in high-overtone g-modes (see Montgomery et al. 2003; Giammichele et al. 2017) also contributes to potential ambiguities in the derived stellar parameters, even when several independent pulsation periods are available. In particular, the number of detected modes is not necessarily indicative of the reliability of the seismological solution; rather, it is their distribution in radial order and the degree of mode trapping that determine the diagnostic power of the dataset.

8. Summary

This study presents an asteroseismic investigation of the ZZ Ceti star WD 1310+583. A prerequisite for asteroseismic modelling is the identification of the star's normal pulsation modes. These modes were derived from 120-second cadence photometric data obtained with TESS, supplemented by relevant parameters available in the literature.

Additional constraints were provided by spectroscopic analysis, based on data collected with the Cosmic Origins Spectrograph onboard the Hubble Space Telescope. We also examined the possible presence of rotationally split multiplets.

By means of an asteroseismic analysis, we derived a suggestive asteroseismological model characterised by the following physical parameters: $M_{*} = 0.632\,M_{\odot}$, $T_{\rm eff} = 11\,702$ K, the stellar mass being compatible with the predictions of the period spacing ($M_{\star} \gtrsim 0.6\,M_{\odot}$). The corresponding asteroseismic distance (27.75 pc) is smaller compared to the geometric distance inferred from Gaia astrometry (30.79 pc).

Continued operation of the TESS mission will enable not only similarly detailed case studies, but also ensemble analyses of white dwarf pulsators and the discovery of new compact variables. Here, we demonstrate the high scientific value of studying white dwarf variables with TESS, and the continuation of these observations would be of great benefit to the white dwarf community.

Acknowledgements. The authors thank the anonymous referee for constructive comments and recommendations on the manuscript. The authors acknowledge Michael H. Montgomery (Department of Astronomy, University of Texas at Austin; McDonald Observatory, Fort Davis) for the useful early discussions. The authors also acknowledge Mukremin Kilic (Homer L. Dodge Department of Physics and Astronomy, University of Oklahoma), Antoine Bedard (Department of Physics, University of Warwick) and Detlev Koester (Institut für Theoretische Physik und Astrophysik, Universität Kiel) for their helpful discussion. Zs.B. and Á.S. acknowledge the financial support of the KKP-137523 'SeismoLab' Élvonal grant of the Hungarian Research, Development and Innovation Office (NKFIH). M.U. gratefully acknowledges support from the Research Foundation Flanders (FWO) through a Junior Postdoctoral Fellowship (grant agreement No: 1247624N). This paper includes data collected with the TESS mission, obtained from the MAST data archive at the Space Telescope Science Institute (STScI). Funding for the TESS mission is provided by the NASA Explorer Programme. STScI is operated by the Association of Universities for Research in Astronomy, Inc., under NASA contract NAS 5–26555.

References

Ahumada, R., Allende Prieto, C., Almeida, A., et al. 2020, ApJS, 249, 3
Althaus, L. G., Córsico, A. H., Isern, J., & García-Berro, E. 2010, A&ARv, 18, 471
Bailer-Jones, C. A. L., Rybizki, J., Fouesneau, M., Demleitner, M., & Andrae, R. 2021, VizieR On-line Data Catalog: I/352
Bédard, A., Bergeron, P., Brassard, P., & Fontaine, G. 2020, ApJ, 901, 93
Bell, K. J., Hermes, J. J., Bischoff-Kim, A., et al. 2015, ApJ, 809, 14
Bell, K. J., Hermes, J. J., Montgomery, M. H., et al. 2016, ApJ, 829, 82
Bell, K. J., Hermes, J. J., Montgomery, M. H., et al. 2017, ASP Conf. Ser., 509, 303
Bell, K. J., Córsico, A. H., Bischoff-Kim, A., et al. 2019, A&A, 632, A42
Bischoff-Kim, A., Montgomery, M. H., & Winget, D. E. 2008, ApJ, 675, 1505
Bognár, Z., Kalup, C., Sódor, Á., Charpinet, S., & Hermes, J. J. 2018, MNRAS, 478, 2676
Bognár, Z., Kawaler, S. D., Bell, K. J., et al. 2020, A&A, 638, A82
Bognár, Z., Sódor, Á., Clark, I. R., & Kawaler, S. D. 2023, A&A, 674, A204
Brickhill, A. J. 1991, MNRAS, 251, 673
Calcaferro, L. M., Córsico, A. H., Uzundag, M., et al. 2024, A&A, 691, A194
Castro-Ginard, A., Penoyre, Z., Casey, A. R., et al. 2024, A&A, 688, A1
Chambers, K. & Pan-STARRS Team 2018, AAS Meet. Abstr., 231, 102.01
Córsico, A. H. 2020, Front. Astron. Space Sci., 7, 47
Córsico, A. H., & Althaus, L. G. 2006, A&A, 454, 863
Córsico, A. H., Althaus, L. G., Miller Bertolami, M. M., & Kepler, S. O. 2019, A&ARv, 27, 7
Cukanovaite, E., Tremblay, P.-E., Bergeron, P., et al. 2021, MNRAS, 501, 5274
De Gerónimo, F. C., Althaus, L. G., Córsico, A. H., Romero, A. D., & Kepler, S. O. 2017, A&A, 599, A21
De Gerónimo, F. C., Althaus, L. G., Córsico, A. H., Romero, A. D., & Kepler, S. O. 2018, A&A, 613, A46
Dolez, N., & Vauclair, G. 1981, A&A, 102, 375
Fontaine, G., & Brassard, P. 2008, PASP, 120, 1043

Fuchs, J. T. 2017, Ph.D. Thesis, University of North Carolina, Chapel Hill
Gaia Collaboration 2022, VizieR On-line Data Catalog: I/355
Gentile Fusillo, N. P., Tremblay, P. E., Jordan, S., et al. 2018, MNRAS, 473, 3693
Gentile Fusillo, N. P., Tremblay, P. E., Cukanovaite, E., et al. 2021, MNRAS, 508, 3877
Giammichele, N., Charpinet, S., Brassard, P., & Fontaine, G. 2017, A&A, 598, A109
Goldreich, P., & Wu, Y. 1999, ApJ, 511, 904
Handler, G., Pikall, H., O'Donoghue, D., et al. 1997, MNRAS, 286, 303
Hermes, J. J., Montgomery, M. H., Bell, K. J., et al. 2015, ApJ, 810, L5
Hermes, J. J., Gänsicke, B. T., Kawaler, S. D., et al. 2017, ApJS, 232, 23
Kawaler, S. D. 1988, IAU Symp., 123, 329
Leggett, S. K., Bergeron, P., Subasavage, J. P., et al. 2018, ApJS, 239, 26
Liebert, J., Bergeron, P., & Holberg, J. B. 2005, ApJS, 156, 47
Montgomery, M. H., Metcalfe, T. S., & Winget, D. E. 2003, MNRAS, 344, 657
Munday, J., Pelisoli, I., Tremblay, P. E., et al. 2024, MNRAS, 532, 2534
O'Brien, M. W., Tremblay, P. E., Klein, B. L., et al. 2024, MNRAS, 527, 8687
O'Donoghue, D. 1994, MNRAS, 270, 222
Ricker, G. R., Winn, J. N., Vanderspek, R., et al. 2015, J. Astron. Telesc. Instrum. Syst., 1, 014003
Sahu, S., Gänsicke, B. T., Tremblay, P.-E., et al. 2023, MNRAS, 526, 5800
Saumon, D., Blouin, S., & Tremblay, P.-E. 2022, Phys. Rep., 988, 1
Tassoul, M., Fontaine, G., & Winget, D. E. 1990, ApJS, 72, 335
Tremblay, P. E., & Bergeron, P. 2009, ApJ, 696, 1755
Tremblay, P. E., Ludwig, H. G., Steffen, M., & Freytag, B. 2013, A&A, 559, A104
Tremblay, P. E., Gianninas, A., Kilic, M., et al. 2015, ApJ, 809, 148
Uzundag, M., Vučković, M., Németh, P., et al. 2021, A&A, 651, A121
Uzundag, M., De Gerónimo, F. C., Córsico, A. H., et al. 2023, MNRAS, 526, 2846
Winget, D. E., & Kepler, S. O. 2008, ARA&A, 46, 157
Winget, D. E., van Horn, H. M., Tassoul, M., et al. 1982, ApJ, 252, L65
Winget, D. E., Nather, R. E., Clemens, J. C., et al. 1991, ApJ, 378, 326
Zima, W. 2008, CoAst, 155, 17

Appendix A: Frequency, period, and amplitude values determined from the TESS datasets.

Table A.1. Frequency, period, and amplitude values determined from the TESS datasets.

	f [μHz]	P [s]	A [mma]	Comments	Lin. comb.
f_{01}	634.0	1577.3	6.6	Bognár et al. (2018)	
f_{02}	668.0	1497.0	1.08	only in s22	
f_{03}	717.4	1394.0	1.07	s22	
f_{04}	927.3	1078.4*	0.98	s4849	
f_{05}	963.0	1038.4*	7.0	Bognár et al. (2018)	
f_{06}	997.2	1002.8	1.70	s22	
f_{07}	1003.0	997.1*	2.41	s22	
f_{08}	1012.6	987.5	1.12	s22	
f_{09}	1017.8	982.5	1.44	s22	
f_{10}	1032.7	968.4	2.98		
f_{11}	1038.3	963.1	2.66	s22	
f_{12}	1041.5	960.1	1.06	s4849	
f_{13}	1044.8	957.2	1.41		
f_{14}	1048.6	953.6*	1.95		
f_{15}	1076.9	928.6	3.69		
f_{16}	1082.6	923.7	1.48	s7576	
f_{17}	1087.8	919.3*	2.08	s7576	
f_{18}	1095.9	912.5	0.85	s4849	
f_{19}	1091.6	916.1	1.14	s7576	
f_{20}	1126.9	887.4	2.37	s7576	
f_{21}	1144.5	873.8*	1.12	s7576	
f_{22}	1149.5	869.9	0.91	s7576	
f_{23}	1183.9	844.7	1.31	s7576	
f_{24}	1193.9	837.6*	10.45	s7576	
f_{25}	1250.3	799.8	2.67	s7576	
f_{26}	1260.3	793.4*	3.94	s7576	
f_{27}	1389.1	719.9	0.86	s1516	
f_{28}	1435.0	696.9	0.97	s1516	
f_{29}	1438.9	695.0	4.74		
f_{30}	1456.0	686.8	1.76	s1516	
f_{31}	1452.6	688.4	1.16	s4849	
f_{32}	1478.9	676.2*	1.08		
f_{33}	1601.3	624.5	0.82	s4849	
f_{34}	1727.9	578.7	1.05	s22	
f_{35}	1751.9	570.8	1.87		
f_{36}	1844.2	542.2	0.78	s4849	
f_{37}	1969.4	507.8*	2.94		
f_{38}	1996.0	501.0	1.21		
f_{39}	2558.3	390.9*	–	Gentile Fusillo et al. (2018)	
f_{40}	2739.0	365.1	2.39		
f_{41}	2759.0	362.4	1.40		
	362.2	2761.2	1.01	s1516	yes (s1516; $f_{29} - f_{15}$)
	404.8	2470.2	0.98		yes (s1516, s22; $f_{29} - f_{10}$)
	775.2	1290.0	1.38	s7576	yes (s7576; $f_{37} - f_{24}$)
	967.5	1033.6	1.07	s22	yes (s22; $f_{37} - f_{07}$)
	1544.9	647.3	1.04	s7576	yes (s7576; $f_{40} - f_{24}$)
	1720.8	581.1	1.89		yes (s22; $f_{40} - f_{09}$)
	2071.0	482.9	1.32		yes (s22; $f_{10} + f_{11}$)
	2183.9	457.9	1.29		yes (s1516; half-int. $1.5 * f_{30}$)
	2387.7	418.8	0.85	s7576	yes (s7576; harmonic $2 * f_{24}$)

Notes. Only three periods are from the literature, which are indicated in fourth column. Where similar frequencies were found in multiple TESS datasets, their amplitude-averaged period is listed in the table. Periods that form a regular pattern of $\ell = 1$ modes with constant period spacing are marked with an asterisk (see Sect. 5). In cases where a significant frequency was found in only one dataset, the sector number is indicated in the fourth column. The fifth column notes if the given frequency was identified as a linear combination in any dataset.

Appendix B: Frequencies, periods, and amplitudes of the detected signals in the datasets of the different sectors.

Table B.1. Results of analysis of sector s15s16 dataset.

	f [μHz]	P [s]	A [mma]
F19	362.2	2761.2	1.0
F32	403.2	2479.9$^+$	0.8
F31	404.1	2474.6$^+$	0.9
F30	405.5	2466.0	0.8
F17	1032.6	968.5$^+$	1.4
F13	1033.2	967.9	1.3
F18	1034.3	966.8$^+$	1.1
F03	1076.2	929.2$^+$	2.3
F10	1076.5	929.0$^+$	1.8
F02	1076.7	928.7	3.2
F09	1077.1	928.5$^+$	2.1
F15	1078.4	927.3$^+$	1.5
F20	1079.3	926.5$^+$	1.1
F25	1389.1	719.9	0.9
F21	1435.0	696.9	1.0
F26	1438.1	695.4$^+$	0.9
F01	1438.9	695.0	5.8
F23	1439.2	694.8$^+$	1.0
F29	1454.3	687.6$^+$	1.1
F08	1455.1	687.2$^+$	2.2
F33	1455.7	686.9$^+$	1.0
F07	1456.0	686.8	1.8
F27	1456.5	686.6$^+$	1.0
F28	1457.7	686.0$^+$	0.9
F24	1478.3	676.4$^+$	1.0
F14	1479.2	676.0	1.0
F12	1721.3	580.9	1.4
F05	1751.9	570.8	2.6
F04	1969.7	507.7	2.7
F16	1995.9	501.0	1.2
F22	2184.0	457.9	1.0
F06	2739.2	365.1	2.5
F11	2759.1	362.4	1.5

Notes. We mark with plus sign frequencies close to arger amplitude peak. In these cases the amplitude determinations are not completely reliable. We did not consider these frequencies as unique ones in the next steps of our frequency analysis.

Table B.2. Results of analysis of sector s22 dataset.

	f [μHz]	P [s]	A [mma]
F31	406.3	2461.5	1.1
F36	668.0	1497.0	1.1
F38	717.4	1394.0	1.1
F37	967.5	1033.6	1.1
F33	996.1	1003.9$^+$	1.2
F13	997.2	1002.8	1.7
F18	1002.0	998.0$^+$	1.6
F07	1003.0	997.1	2.4
F09	1003.8	996.2$^+$	2.1
F34	1012.6	987.5	1.1
F21	1017.8	982.5	1.4
F23	1030.6	970.3$^+$	1.3
F02	1032.6	968.4	5.2
F22	1033.7	967.4$^+$	1.3
F12	1037.4	964.0 $^+$	1.7
F04	1038.3	963.1	2.7
F11	1039.3	962.2$^+$	1.9
F32	1040.3	961.2$^+$	1.2
F26	1043.2	958.6$^+$	1.3
F35	1044.0	957.9$^+$	1.2
F16	1045.1	956.8	1.7
F17	1046.2	955.9$^+$	1.5
F27	1047.1	955.0$^+$	1.3
F08	1048.1	954.1	2.3
F14	1049.2	953.1$^+$	1.7
F15	1050.2	952.2$^+$	1.6
F25	1051.2	951.3$^+$	1.4
F19	1075.8	929.6$^+$	1.5
F03	1076.8	928.7	3.6
F20	1077.8	927.8$^+$	1.5
F01	1438.9	695.0	7.2
F29	1721.1	581.0	1.2
F39	1727.9	578.7	1.1
F10	1751.7	570.9	2.0
F05	1969.6	507.7	2.5
F30	1995.6	501.1	1.1
F24	2071.0	482.9	1.3
F40	2072.0	482.6$^+$	1.0
F28	2183.8	457.9	1.2
F06	2739.0	365.1	2.4

Table B.3. Results of analysis of sector s48s49 dataset.

	f [μHz]	P [s]	A [mma]
F34	402.7	2483.2	1.0
F35	927.3	1078.4	1.0
F52	1031.4	969.6$^+$	0.8
F08	1032.6	968.5	2.4
F14	1032.7	968.3$^+$	1.6
F24	1033.7	967.4$^+$	1.2
F33	1034.2	966.9$^+$	1.1
F49	1040.0	961.5$^+$	0.9
F50	1041.2	960.4$^+$	1.0
F48	1041.5	960.1	1.1
F36	1044.2	957.6	1.2
F51	1044.5	957.4$^+$	0.9
F18	1046.4	955.6$^+$	1.7
F19	1047.7	954.5$^+$	1.6
F46	1048.1	954.1$^+$	1.0
F39	1049.2	953.1$^+$	1.2
F15	1049.3	953.0	1.6
F41	1049.7	952.6$^+$	1.2
F26	1050.3	952.1$^+$	1.2
F17	1050.8	951.6$^+$	1.2
F23	1052.0	950.6$^+$	1.6
F38	1052.4	950.2$^+$	1.2
F30	1053.8	948.9$^+$	1.2
F27	1055.1	947.8$^+$	1.2
F16	1074.8	930.4$^+$	1.7
F10	1075.7	929.6$^+$	3.1
F02	1076.0	929.3$^+$	3.8
F03	1076.6	928.8$^+$	4.2
F01	1077.2	928.3	4.2
F07	1077.4	928.2$^+$	3.1
F43	1078.3	927.4$^+$	1.0
F11	1078.5	927.2$^+$	2.1
F42	1095.9	912.5	0.9
F44	1127.7	886.8$^+$	0.9
F21	1128.7	886.0$^+$	not valid
F12	1128.7	885.9$^+$	not valid
F06	1129.2	885.6	2.7
F32	1129.4	885.4$^+$	1.5
F47	1438.3	695.3$^+$	0.8
F25	1438.8	695.0	1.2
F37	1452.6	688.4	1.2
F54	1453.3	688.1$^+$	0.9
F55	1457.8	686.0$^+$	0.8
F31	1478.1	676.5	1.1
F28	1478.6	676.3	1.1
F45	1601.3	624.5	0.8
F04	1720.8	581.1	3.0
F40	1751.7	570.9$^+$	1.0
F13	1751.9	570.8	1.7
F53	1844.2	542.2	0.8
F05	1969.3	507.8	2.6
F29	1995.9	501.0	1.1
F22	2183.9	457.9	1.3
F09	2738.9	365.1	2.3
F20	2758.9	362.5	1.4

Notes. Not valid amplitudes mean that we detect two frequencies so close to each other that we cannot resolve them correctly.

Table B.4. Results of analysis of sector s75s76 dataset.

	f [μHz]	P [s]	A [mma]
F34	1082.2	924.1$^+$	1.2
F15	1082.6	923.7	1.5
F39	1085.2	921.5$^+$	1.1
F19	1087.1	919.9$^+$	1.7
F18	1087.8	919.3	2.1
F42	1091.1	916.5$^+$	1.0
F28	1091.6	916.1	1.1
F06	1126.8	887.4	not valid
F09	1126.8	887.4$^+$	not valid
F24	1127.2	887.2$^+$	1.6
F48	1129.8	885.1$^+$	1.0
F36	1131.0	884.2	1.1
F35	1133.6	882.2$^+$	1.2
F32	1133.9	881.9	1.3
F43	1144.5	873.8	1.1
F46	1145.0	873.4$^+$	1.1
F49	1149.5	869.9	0.9
F22	1183.9	844.7	1.3
F31	1184.4	844.3$^+$	1.6
F38	1185.0	843.9$^+$	1.4
F37	1186.0	843.2$^+$	1.3
F45	1188.1	841.7$^+$	1.1
F20	1190.9	839.7$^+$	1.5
F51	1192.9	838.3$^+$	1.2
F03	1193.7	837.7$^+$	8.6
F01	1193.9	837.6	10.4
F02	1194.2	837.4$^+$	7.9
F10	1195.4	836.6$^+$	2.4
F44	1195.5	836.4$^+$	1.3
F07	1196.6	835.7	2.2
F16	1197.1	835.3$^+$	not valid
F13	1197.1	835.3$^+$	not valid
F41	1245.2	803.1$^+$	1.0
F12	1250.0	800.0$^+$	2.1
F11	1250.3	799.8	2.7
F27	1251.7	798.9$^+$	1.4
F21	1260.3	793.4$^+$	not valid
F04	1260.3	793.4	not valid
F50	1261.7	792.6$^+$	1.0
F29	1263.0	791.8$^+$	1.4
F23	1263.6	791.4$^+$	1.8
F47	1264.1	791.1$^+$	1.0
F40	1544.9	647.3	1.0
F14	1720.3	581.3	1.9
F33	1752.5	570.6	1.2
F05	1969.2	507.8	3.9
F25	1996.4	500.9	1.4
F17	2184.0	457.9	1.7
F52	2387.7	418.8	0.9
F08	2739.0	365.1	2.3
F30	2759.0	362.5	1.3
F26	775.2	1290.0	1.4